Heliyon 10 (2024) e29666

Contents lists available at ScienceDirect

Heliyon

journal homepage: www.cell.com/heliyon

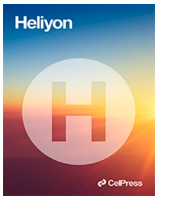

Research article

Design of dissimilar material joint for defect-free multi-material additive manufacturing via laser-directed energy deposition

Qing-Ye Jin [a], Hyunji Nam [a], Haeju Jo [a], Jiyoung Park [a], Ho Ju Kang [b], Dong Joo Kim [b], Wookjin Lee [a,*]

[a] School of Materials Science and Engineering, Pusan National University, Busan, 46241, Republic of Korea
[b] Technical R&D Center, Seo Yeong Co., LTD., Busan, 46744, Republic of Korea

ARTICLE INFO

Keywords:
Laser-directed energy deposition
Multi-material additive manufacturing
Digital image correlation

ABSTRACT

Additive manufacturing technology has advanced beyond creating optimized features, from strengthening materials to make them lightweight to fabricating multi-material combinations that offer functionalities beyond the capabilities of individual materials. In this study, a lamination method for laser-directed energy deposition (LDED) is developed to achieve dense multi-material features, and a design that combines different and dissimilar materials is developed. To evaluate these novel developments, two materials—AISI 316L stainless steel and Inconel 625—are introduced. Tensile specimens, fabricated via multi-material additive manufacturing using LDED, are subjected to tensile tests that are recorded on video for digital image correlation. After the tests, fracture surface analyses of the fractured specimens are performed via scanning electron microscopy, and optical monitoring analyses are performed on the specimens that are not subjected to the tensile tests. The results indicate that the specimens demonstrate varied mechanical properties due to the influence of lamination direction and order, which affect the formation of critical cracks and pores.

1. Introduction

Additive manufacturing (AM) is a well-known advanced manufacturing technology that can fabricate complex structures without exponentially increasing the processing difficulty or cost [1]. This is because AM involves laminating two-dimensional (2D) features layer-by-layer to obtain the final three-dimensional (3D) feature. AM can achieve increasingly complex designs by optimizing geometrical structures such as the topology or lattice structures [2–5] [2–5] [2–5]. However, optimizing features is not sufficient to satisfy all specified conditions, such as ultimate strength, corrosion resistance, and electrical conductivity [6–8] [6–8] [6–8]. Metal AM is usually performed using a single metallic material with a near-uniform chemical composition. AISI 316L stainless steel and Ni-based Inconel 625 are typical examples of these materials [9–14].

Multi-material AM (MMAM) can be used to fabricate parts with multiple materials having optimized complex geometries [15]. The advantages of multi-material composites, such as metal–metal composites, are highly varying, outstanding, and well-known. However, metallic bonding limits the conventional process for producing metal–metal composites. Metallic materials are strong and reliable because a considerable amount of energy is required to break their metallic bonds [8]. Therefore, bonding two different metallic

* Corresponding author.
E-mail address: wookjin.lee@pusan.ac.kr (W. Lee).

https://doi.org/10.1016/j.heliyon.2024.e29666
Received 10 July 2023; Received in revised form 11 April 2024; Accepted 12 April 2024

materials requires a high-energy source, such as a laser, electron beam, or arc [16]. Furthermore, the conventional metal–metal composite manufacturing methods, such as welding, brazing, and plating, are unsuitable. The advantages and disadvantages of conventional methods have been well established for over a century. Welding is convenient and efficient for connecting two parts; however, it is unsuitable for large-area bonding or feature creation. Brazing can achieve efficient large-surface bonding; however, it is difficult to bond pieces that are too small or large for the machine clamp. Plating can accurately deposit a metal layer upon a surface; however, it is inefficient if the layer thickness exceeds the millimeter range. MMAM, which is the focus of this study, can directly fabricate 3D features with different materials instead of bonding two parts.

Laser-directed energy deposition (LDED) is a well-known AM technology that jets powder with shield gas from the nozzle and melts the powder using a laser at the central axis of the nozzle. LDED exhibits several advantages over other AM processes, such as convenient and fast powder control, fast lamination, and microstructure refinement, which are relevant to material lamination. Therefore, LDED is considered one of the most suitable AM methods for MMAM [17]. Heer et al. [18] fabricated a magnetic–nonmagnetic bimetallic structure using LDED. Putra et al. [19] fabricated a micro lattice structure for bone-cell growth using Ti-, Mg-, and Fe-based biomaterials. Sagong et al. [20] examined the properties and microstructure of Fe–Ni multi-material structures, comprising AISI 316L and Inconel 718, fabricated via LDED. They fabricated tensile specimens by directly laminating Inconel 718 onto AISI 316L. These specimens were then tested horizontally by simultaneously stretching both materials. This approach aimed to examine the combined characteristics of MMAM, a departure from previous studies that focused solely on the combined performance of MMAM.

In this study, designs were developed for fabricating multi-material parts via LDED, where two different metals—Fe-based AISI 316L stainless steel (316L) and Ni-based Inconel 625 (In625)—were interlocked. Recent works regarding a joint between Fe- and Ni-based alloys directly by LDED have progressed to a certain level [21–25]. However, most of the works have focused on simple vertical connection by laminating one material upon the other one. This study aims to optimize the shape of interface geometry between the dissimilar materials, ensuring a defect-free joint, and develop functional designs that mechanically interlock two dissimilar materials through LDED. One design was V-shaped (V) to prevent the laminated features from obstructing the lamination of other materials. The other was an anchor, with a combination of Vs, which interlocked the other material, enabling the mechanical connection of dissimilar materials. To estimate the mechanical properties of the structures fabricated via LDED, all fabricated specimens were subjected to tensile testing. Digital image correlation (DIC) was performed to analyze, in detail, the deformation behavior of the multi-material specimens during the test [26]. In addition to DIC, fracture surface analyses using scanning electron microscopy (SEM) and optical monitoring (OM) of the untested specimens were performed. Following fracture surface analysis, the specimens could be roughly classified into two categories: those that exhibited fracturing at the interface of 316L–In625 and those that exhibited fracturing from 316L [27].

In one of the recent MMAM studies, which is about interface geometry, structure and mechanical properties of a slopped interface between AISI 316L and Inconel718 was studied [25]. In the study, the material was switched between two different materials in every LDED layer to complete a dense multi-material feature. The tensile properties of the multi-material features produced by this method were compared with the identically designed structures but produced by LDED deposition of Inconel718 followed by 316L deposition and surface machining. The results showed inferior tensile properties of the features produced by switching the material in every layer in comparison to the features produced by depositing the materials one by one without switching, due to the complexity of the interface shape produced by switching the material in each layer. In addition, switching the material in every layer requires the powder-supply device to switch from one powder to another in every layer, which is time-consuming. In addition, undesired mixing of

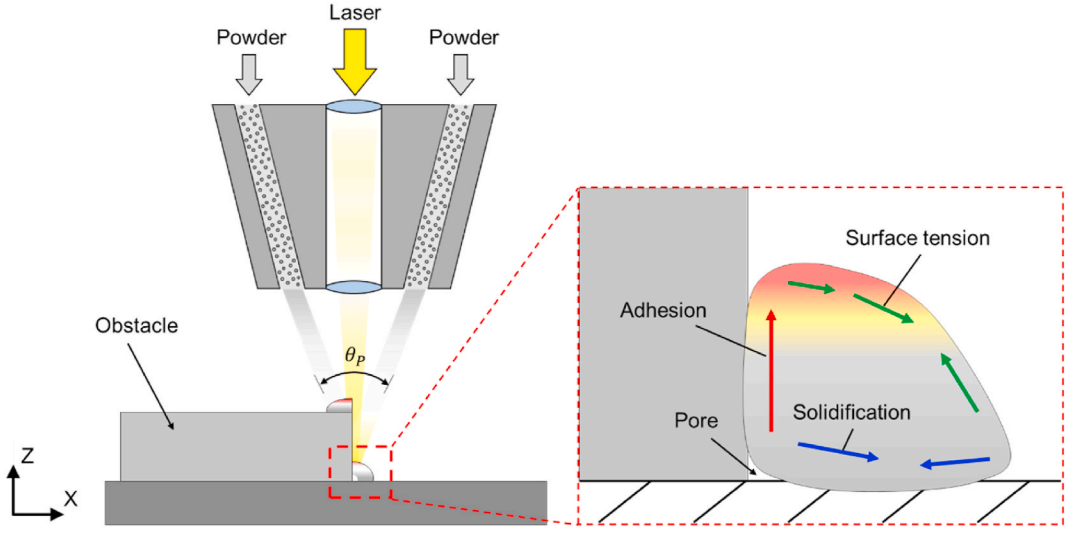

Fig. 1. Schematic of direct-energy deposition (DED) lamination when obstructed by formerly laminated material and its convention flow inside the melted powder.

powder may occur because a small amount of powder may remain in the powder-supply system after switching the device. Moreover, mixing of different metal powders in the jetting nozzle may possibly cause unstable powder supply or even nozzle clogging. Therefore, it is desire to develop a process to minimize switching of material during LDED.

When multiple layers of one material is deposited first and then the second material are deposited to minimize the switching, interface geometry and deposition sequence have to be carefully selected to avoid process-inherent defect formation. An improper design of LDED may occur critical process-inherent defects. One of the primary reasons for these critical defects is the 'obstacle effect,' where previously laminated features hinder the lamination of subsequent materials, as illustrated in Fig. 1. This obstruction hinders powder jetting, causing the molten metal to flow downward and stretch the surface in contact with the obstacle due to adhesion. The surface in contact with the base metal contracts upon solidification, while other surfaces contract due to surface tension [28–31]. Consequently, pores form between the different metals due to convection flow within the molten metal.

2. Design of multi-material structures for LDED

A V-shaped design was developed to prevent these types of defects by minimizing the switching of materials, as shown in Fig. 2 (a). The figure shows the lamination order along with the number of switches. Specifically, the number of switches is 2, and θ_V denotes the angle of V, which is the angle of the interface between two materials. The design can be approximately classified into two cases depending on the size of θ_V and θ_P (shown in Fig. 1)—one where $\theta_V < \frac{\pi-\theta_P}{2}$ and the other where $\theta_V > \frac{\pi-\theta_P}{2}$, where $\frac{\pi-\theta_P}{2}$ is the angle where powder jetting starts to overlap with previously deposited material A, as shown in Fig. 2. Theoretically, the former case presents no obstacle to powder jetting, whereas the latter does. When θ_V exceeds $\frac{\pi-\theta_P}{2}$, the powder jetting route is clearly obstructed by the previously laminated slope on the left, which is colored green, as shown in Fig. 2 (b). To analyze the combined quality of AM, according to θ_V, three angles (30°, 45°, and 60°) are considered in this study. Given that $\theta_P = 80°$, the order of the angles, according to size, is as follows: $30° < 45° < \frac{\pi-\theta_P}{2} = 50° < 60°$.

Additionally, to interlock dissimilar materials, an anchor is designed by combining Vs with different angles, as shown in Fig. 3. Specifically, the V that mechanically connects the two materials has an angle of θ_{V2}. Reducing the angle without changing other parameters can increase the shear section when tensile deformation is applied along the X-axis in the figure. Therefore, θ_{V2} should be as small as possible. Furthermore, other Vs, whose angles are θ_{V1} and θ_{V3}, are designed for homogeneity. To design the anchor efficiently, it should be downsized such that θ_{V1} and θ_{V3} are as large as possible. Therefore, they are designed as follows: $\theta_{V1} = 60°$, $\theta_{V2} = 30°$, and $\theta_{V3} = 60°$. Additionally, the heights of the anchors (H_1, H_2, and H_3) are designed for convenience. The design parameter L_1 is the total length of the conjunction design based on the anchor. This can be expressed using **Eq. (1)**.

$$L_1 = (H_1 + H_2)\tan^{-1}\theta_{V1} + H_2\tan^{-1}\theta_{V2} + (H_2 + H_3)\tan^{-1}\theta_{V3} \tag{1}$$

Given that $H_1 = H_2 = H_3$ and $\theta_{V1} = \theta_{V3} = \frac{\pi}{2} - \theta_{V2} = 60°$, **Eq. (1)** can be reformulated as follows:

$$L_1 = \frac{7\sqrt{3}}{3}H_1 \tag{2}$$

Eq. (2) indicates that the total length of the anchor depends on its width. As each specimen is designed to contain one anchor, the length of the anchor depends on the height of the specimen.

To compare with the V-type design, a simple bonding approach was introduced, designed by maximizing θ_V to $\theta_V = 90°$. This approach was implemented under different building conditions when laminating horizontally and vertically. In horizontal lamination, the scenario is similar to that shown in Fig. 1, where a typical obstacle hinders the lamination of the other material. In vertical lamination, however, the scenario is akin to laminating on a base plate, with the key difference being the composition of the base plate.

The designs for comparison, except for the simple bonding case, are presented in Fig. 4. The T-type structure is designed such that

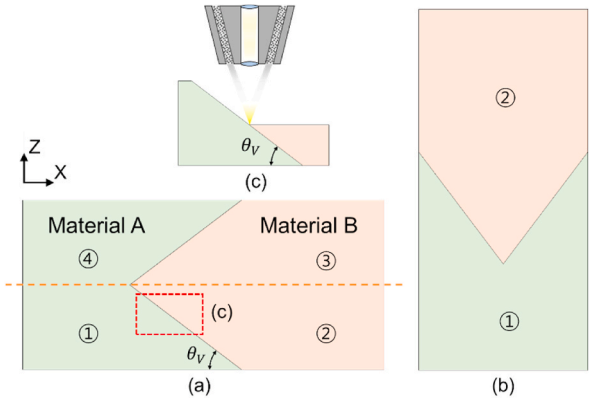

Fig. 2. V-shaped design wherein the building direction is (a) horizontal and (b) vertical, presenting the lamination order for MMAM and (c) lamination procedure of the specific region marked in (a).

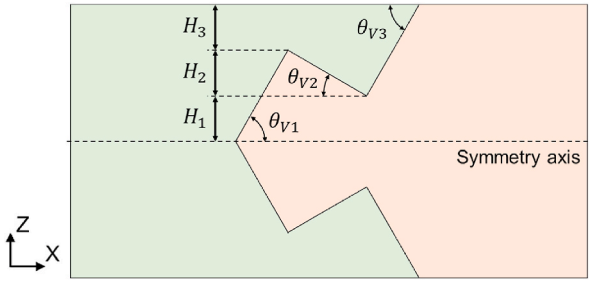

Fig. 3. Design of a horizontal anchor that is a combination of various Vs and its design parameters.

only the interfaces of the two materials are connected, as shown in Fig. 4 (a). For comparison, L_1 is designed to be equal to that of the anchor. For convenience, parameters H_4 and H_5 are designed to be equal and are the double the value of H_1. The other hammer-type design used for comparison, as shown in Fig. 4 (b), is geometrically designed to exhibit performance that is similar to or better than that of the anchor. This is also a comparison design with the same value for L_1. For convenience, the parameters are designed such that $L_2 = \frac{1}{2}L_1$ and $H_6 = \frac{1}{2}H_4$. Both designs have the same total height as the anchor. Theoretically, if the comparison designs were fabricated densely under ideal conditions, then the performance of the specimens would match that of the V-shaped design and anchor. However, owing to the manufacturing characteristics of LDED, the perpendicular components at every interface of the two materials can impede lamination, as illustrated in Fig. 1. Consequently, the comparisons were conducted while disregarding the impact of this obstruction.

3. Experiment

To evaluate the performance of the various designs described in Section 2, a tensile test was chosen. This test is conducted to assess the structural characteristics and performance of both the V-type and anchor joints. Therefore, simple bar-type specimens were produced and subjected to the tests. The tensile directions were determined based on the geometrically weakest points: the X-axis for horizontal specimens and the Z-axis for vertical specimens. To prepare specimens for the tensile test, a bulk feature laminated by LDED in its as-built state was fabricated and then sliced into simple bar shapes containing the designed interfaces.

3.1. LDED process parameters

The bulks were manufactured by MX-lab (Insstek Co., Korea) with a powder jetting angle $\theta_P = 80°$, a laser focusing length $H_P = 11.4$ mm, and a laser diameter $D_L = 0.4$ mm. The installed laser was a ytterbium-fiber laser. Two types of materials were used for AM: gas-atomized spherical 316L powder with a particle size of 63–108 μm and gas-atomized spherical In625 powder with a particle size of 57–109 μm. In AM, the processing parameters were adjusted based on the type of powder used, with each powder type having its own permissible range. To facilitate continuity and convenience in manufacturing, some overlap in the processing parameters of the two metals was allowed. Common parameters included a laser power $W_L = 190$ W, hatch space $h = 0.3$ mm, and layer thickness $th = 0.15$ mm. The scan speed S_{SS} varied between the materials: for 316L, $S_{SS} = 1080$ mm/min, and for In625, $S_{IN} = 840$ mm/min. To ensure reliability, at least three specimens must be tested; therefore, the thickness of the fabricated features had to be greater than that of the three specimens and four wire-cutting paths. Therefore, the total thickness of the samples was fixed at 9 mm.

The LDED process parameters for 316L and In625 were obtained from previous studies on the performance of 316L and In625 fabricated using the aforementioned LDED machine [32,33]. Table 1 shows the mechanical performances of the two materials manufactured using LDED.

3.2. Design parameters

For the tensile tests, a universal testing machine, QUASAR 50 (Galdabini Co., Italy), was used. This machine has a maximum load

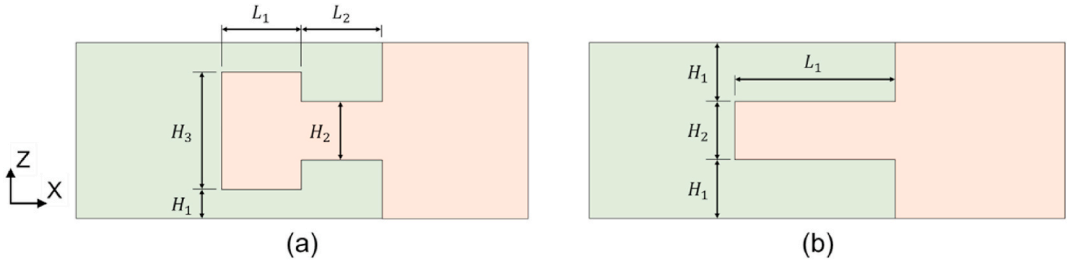

Fig. 4. Design of comparison specimens and their design parameters: (a) T-type and (b) hammer-type.

Table 1
Mechanical performance of AISI 316L and Inconel 625 manufactured by LDED [32,33].

Material	Building direction	Yield strength (MPa)	Tensile strength (MPa)	Maximum tensile elongation (%)
AISI 316L	Horizontal	469	639	50.9
	Vertical	423	641	51.2
Inconel 625	Horizontal	772	1140	35.5
	Vertical	596	983	50.1

capacity of 50 kN and an accuracy of ±0.5 %. Since a claw-type clamp was used to secure the specimens, the fabricated features were sliced into thin-plate specimens, measuring 30 mm in length, 9 mm in width, and 2 mm in thickness. The detailed design parameters of these specimens can be derived from the general design parameters outlined in **Section 2**. Table 2 provides a list of these calculated design parameters.

The specimens used in the manufacturing process are listed in Table 3. They vary according to the design type and building direction. There are three types of specimens (V, anchor, and simple) and two building directions (horizontal and vertical). These specimens are designated by a combination of their type and characteristics, as shown in the sample designation, except in the cases of horizontal and vertical simple bonding. In these cases, the interface between 316L and In625 is flat (i.e., $\theta_V = 90°$). When this geometry is laminated horizontally, the material that is processed first hinders the processing of the next material, as shown in Fig. 1. In the case of vertical lamination, In625 was similarly directly laminated on 316L. These are designed by disregarding the obstruction phenomenon for comparison with V. Therefore, they are designated as simple bonding.

The specimens are illustrated in Fig. 5. As they are manufactured using the LDED process, when the direction of the specimen changes, the lamination strategy should be changed, as described in **Section 2**. In the figure, the formally laminated material is depicted in green, and its sample ID is labeled under its features. As the interface between two materials was always perpendicular, the clamping of the tensile bars was made at one side on the 316L (bottom part of each tensile bar) and at the other side on the In625 (top part of each tensile bar).

The as-built bulk samples manufactured via LDED are presented in Fig. 6. Fig. 6 (a) and (b) shows horizontal and vertical bulk samples of simple bonding ($\theta_V = 90°$) and V-type. Fig. 6 (c) shows anchor type bulk samples and Fig. 6 (d) shows T- and Hammer type bulk samples. It is evident that the V-type, with $\theta_V = 30, 45,$ and $60°$ and anchors have been fabricated well, without any visible defect in naked eyes. In contrast, simple horizontal bonding, Ts, and the hammer-type exhibit critical defects. Therefore, the comparison specimens were omitted in this study, except for the horizontal simple bonding, which is considered representative of the sample. They are then sliced by wire cutting, as shown in Fig. 7. Fig. 7 (a) shows sliced V-type specimens with different θ_V and Fig. 7 (b) shows horizontal simple bonding specimen. Fig. 7 (c), (d) and (e) show anchor, hammer and T-type sliced specimens, respectively. This produced the same result as Fig. 6—no apparent defects are observed in the Vs and anchors (shown in Fig. 6 (a) and (c)); however, the other ones are not.

3.3. Tensile test

The specimens were stretched at the same machine cross-head speed of 0.5 mm/min (strain rate of approximately 0.004 s^{-1}) until fracture and were filmed with a video camera, NemoCAM-300(KOPAS, Korea), for DIC. Furthermore, DIC is an important and widely used noncontact technique for measuring material deformation. Specifically, Ncorr, the DIC software used in this study, is an open-source subset-based 2D DIC package [27]. The algorithm calculates the relative displacement and orientation of a specific point in a material by recognizing its patterns and tracking them from a previous image [34,35]. Given that the patterns of sliced specimens are important and unclear, as shown in Fig. 7, they are painted with DIC spray, which aids the algorithm in recognizing the patterns.

4. Experimental results

Fig. 8 shows the fracturing of the specimens. Fracturing was divided into three steps: (1) necking limit before crack detection; (2) crack expansion limit before fracture; and (3) fracture. The first step shows the specimens' plastic deformation performance and its limitations. The second step indicates the starting point of the crack and its growth direction. The final step shows the fracture interface, which indicates the growth of the crack and fracture type. The stretching distances are recorded and are shown in the figure

Table 2
Design parameters of the specimens.

Design	Type	Design parameter	Value
V		θ_V	30, 45, 60°
Anchor		H_1, H_2, H_3	1.5 mm
		L_1	6.06 mm
Simple	Simple bonding	θ_V	90°
	T-type	H_4, H_5	3 mm
	Hammer-type	H_6	1.5 mm
		L_2	3.0 mm

Table 3
Variations in tensile test specimens manufactured via LDED and abbreviations.

Type	Building direction	Sample design	Sample ID	Sample designation
V	Horizontal	$\theta_V = 30, 45, 60$ °	30h, 45h, 60h	V-type
	Vertical		30v, 45v, 60v	
Anchor	Horizontal	Anchor	Ah	Anchor
	Vertical		Av	
Simple	Horizontal	$\theta_V = 90°$, T, Hammer	90h, Th, Hh	Simple bonding, T, hammer
	Vertical		90v, Tv, Hv	

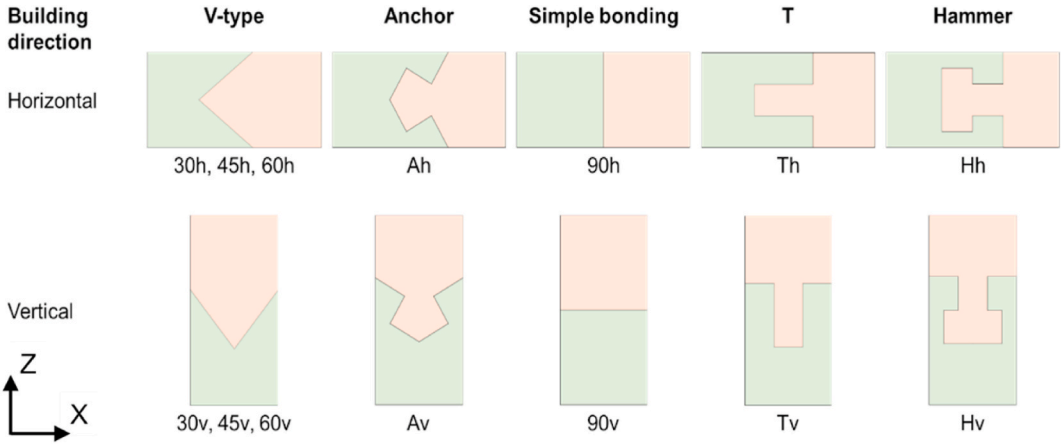

Fig. 5. Tensile test specimen types and their sample IDs.

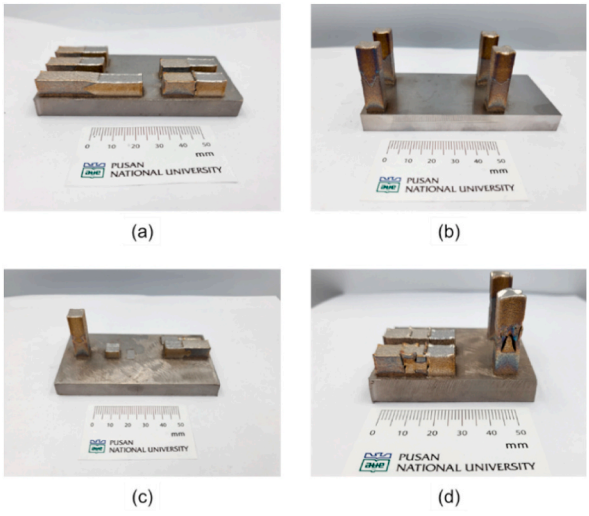

Fig. 6. The multi-material blocks fabricated via LDED: (a) horizontally laminated V-type specimens ($\theta_V = 30°$, 45°, and 60°) and simple bonding specimen; (b) vertically laminated V-type specimens and simple bonding specimens; (c) anchor specimens; (d) T-type and hammer-type specimens.

below. Fig. 8 (a) shows the fracturing of a horizontally laminated V-type specimen at an angle of 30°. Fig. 8 (b) and (c) show the fracturing of specimens whose θ_V are 45° and 60°, respectively. Fig. 8 (d), (e), and (f) show the fracturing of the vertical V-type specimens with angles of 30°, 45°, and 60°, respectively. Fig. 8 (g) shows the fracturing of horizontal simple bonding specimens, and Fig. 8 (h) shows that of the anchor; however, it is divided into four steps. The first and last steps are the same as those of the others; however, the middle step is divided by the direction of crack growth. Fig. 8 (i) and (j) show the simple vertical bonding and vertical anchor specimens, respectively.

The fracture aspect clearly differs from its lamination direction. All the vertically laminated specimens exhibit a general ductile fracture of a single material, 316L, as shown in Fig. 8 (d), (e), (f), (i), and (j). However, fractures of horizontally laminated specimens

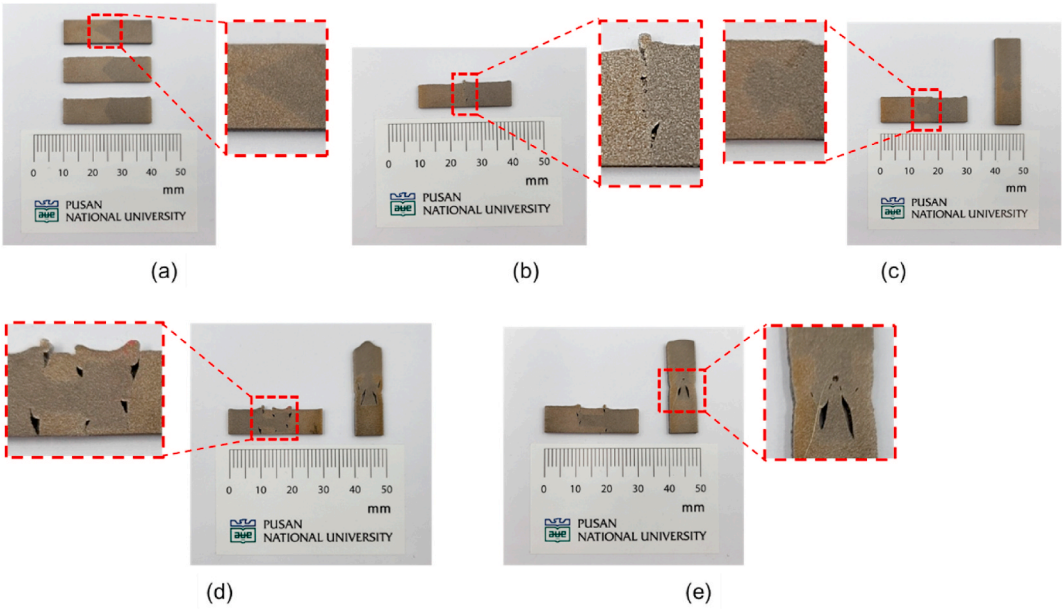

Fig. 7. Sliced thin-plate specimens for the tensile test: (a) V-type specimens at angles of 30°, 45°, and 60°; (b) horizontal simple bonding specimen; (c) anchor specimens; (d) hammer specimens; and (e) T specimens.

are observed to be associated with the interface of the two different materials, such as θ_V. When the angle satisfies $\theta_V < \frac{\pi-\theta_p}{2}$ ($\theta_V = 30\,^\circ$), the fracture begins from the tip of V and propagates through 316L until reaching the end, as shown in Fig. 8 (a). When $\theta_V \approx \frac{\pi-\theta_p}{2}$ or $\theta_V > \frac{\pi-\theta_p}{2}$ ($\theta_V = 45\,^\circ$ and 60°), the fracture begins from one side of the interface, propagates along the interface, and ends at the fracture on the other side of 316L, as shown in Fig. 8 (b) and (c). However, when $\theta_V = 90\,^\circ$, a fracture occurs at one end of the interface and propagates quickly along the interface until it reaches the other end, as shown in Fig. 8 (g). In the case of the anchor, it originates from one end of the interface, grows along it, and then passes through 316L and In625 sequentially and directly, as shown in Fig. 8 (h).

The results of the tensile tests are presented in Fig. 9. The strength and elongation indicated in the figures are macroscale strength and elongation since the multi-material specimens cannot represent a single material property. In the case of the V-type specimens, the horizontally and vertically laminated specimens show entirely different results, as shown in Fig. 9 (a). The vertical specimens exhibit consistently good performance for 316L. All the strain rates of the verticals have exceeded 60 % and the strengths have over 600 MPa, as shown in Fig. 9 (c). However, for the horizontal specimens, the tensile strength and elongation tends to decrease as the angle increases. Excluding the specimens at 60°, the horizontal V-type specimens performed higher strength than the vertical specimens. The results for the anchor specimens are presented in Fig. 9 (b). If the anchor works ideally, then it should perform the same strength as LDED-processed 316L. The vertical anchor exhibits performance similar to that of the V specimens, implying that it works ideally. However, the horizontal anchor unexpectedly performs much worse than the vertical anchor. The tensile strength in this case was about 450 MPa, which is lower than any of V-type specimens. The elongation in this case was ~20 % which is lower than the vertical anchor or any of V-types as shown in Fig. 9 (d). This implies that the horizontal anchor has lost its function.

5. Discussions

The specimens in this study were fabricated using the novel lamination strategy outlined in Section 2. Among various strategies tested, V-shaped designs produced in vertical direction in this study were similar to the ones used in a previous study of Melzer et al. [25], where AISI 316L and Inconel718 alloys with sloped interface geometries by alternating material deposition layer-by-layer in the vertical direction were produced and tested. In the above study, they found that the maximum elongation decreases significantly with increasing the incline angle of the interface when alternating the material in every layer, due to the increase of the porosity defects. The results of present study indicated that the strength and the elongation can remain nearly unchanged if the inclined interfaces are introduced with the novel lamination strategy, as used in V-shaped designs produced in vertical direction, as shown in Fig. 9 (d). This was thought to be because the porosity defect formed by the obstacle effect was effectively prevented by the lamination strategy developed in this study.

The mechanical performance of a metal is generally evaluated based on its deformation characteristics in tensile tests, including elastic, plastic, and fracture deformation regions. Given that the elastic modulus, plastic modulus, and strain are known, the mechanical performance, including the strength, elongation, and work-hardening rate, can be calculated. Although these can be easily determined from calculations before or during small necking, when the specimen narrows critically or fractures, it is difficult to calculate the accurate performance of the material. Additionally, the extreme performance of metallic materials generally occurs after

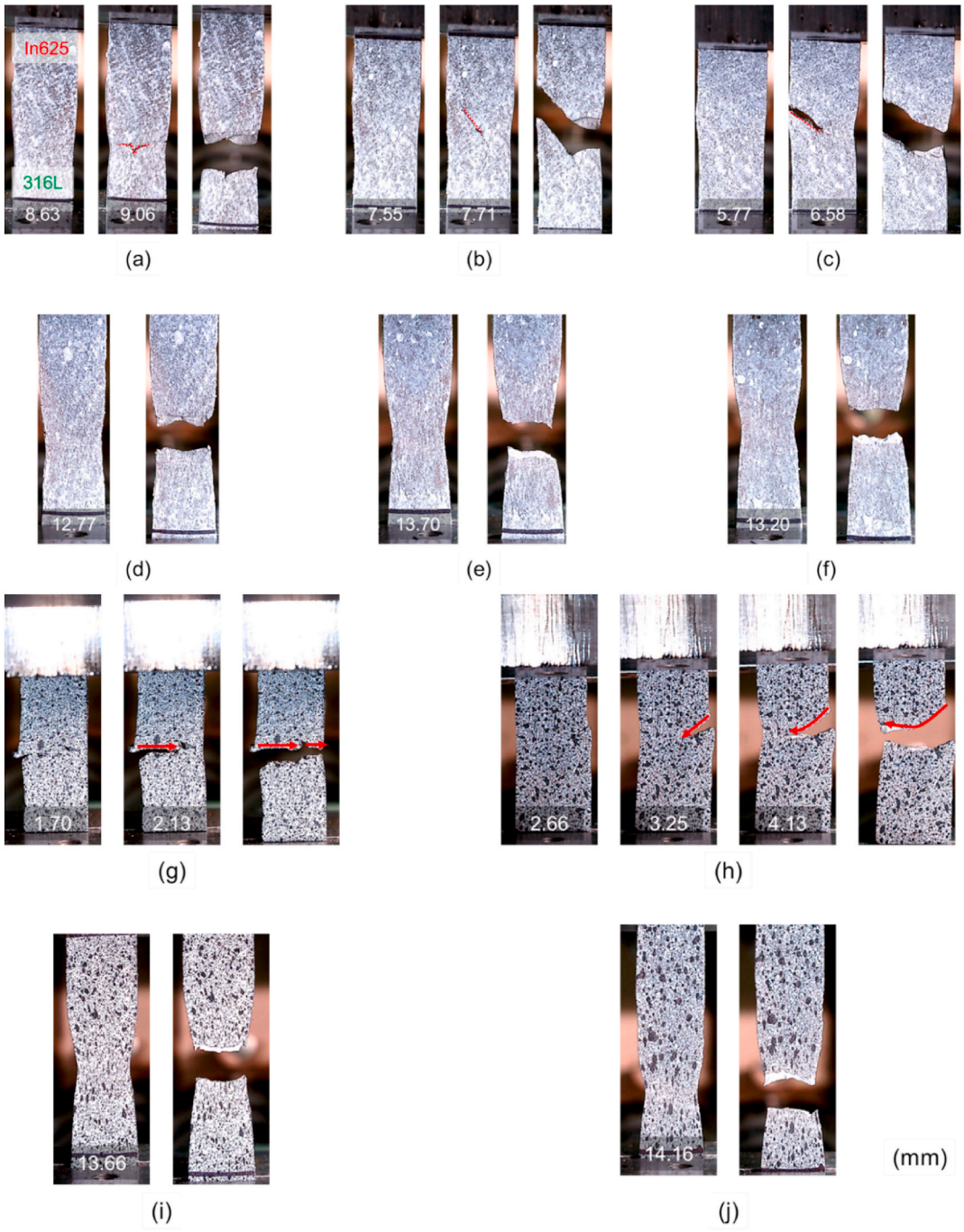

Fig. 8. Fracture procedure of the specimens. Inserted numbers are corresponding deformations (mm) recoded during tensile tests: (a) horizontally laminated V-type specimens with $\theta_V = 30°$, (b) 45°, (c) 60° and (d) vertically laminated specimens with $\theta_V = 30°$, (e) 45°, (f) 60°; (g) horizontal simple bonding specimen; (h) horizontally laminated anchor specimen; (i) vertical simple bonding specimen, and (j) vertically laminated anchor specimen.

the tensile strength point, which is critically narrowed by necking and impending fracture. The potential performance of a material can be determined by its extreme performance, and the goal of the design is to determine the potential of all the materials in the structure. The deformation characteristics under extreme conditions can be inferred from the fracture surface analysis by observing the SEM image of the fracture surface, as shown in Fig. 10.

Based on the behavior of the fracture shown in **Section 3**, it is clear that the vertically laminated specimens exhibit ductile fracture, and a significant number of small dimples are observed on the fracture surface, as shown in Fig. 10 (d), (e), (f), (i), and (j) and in higher

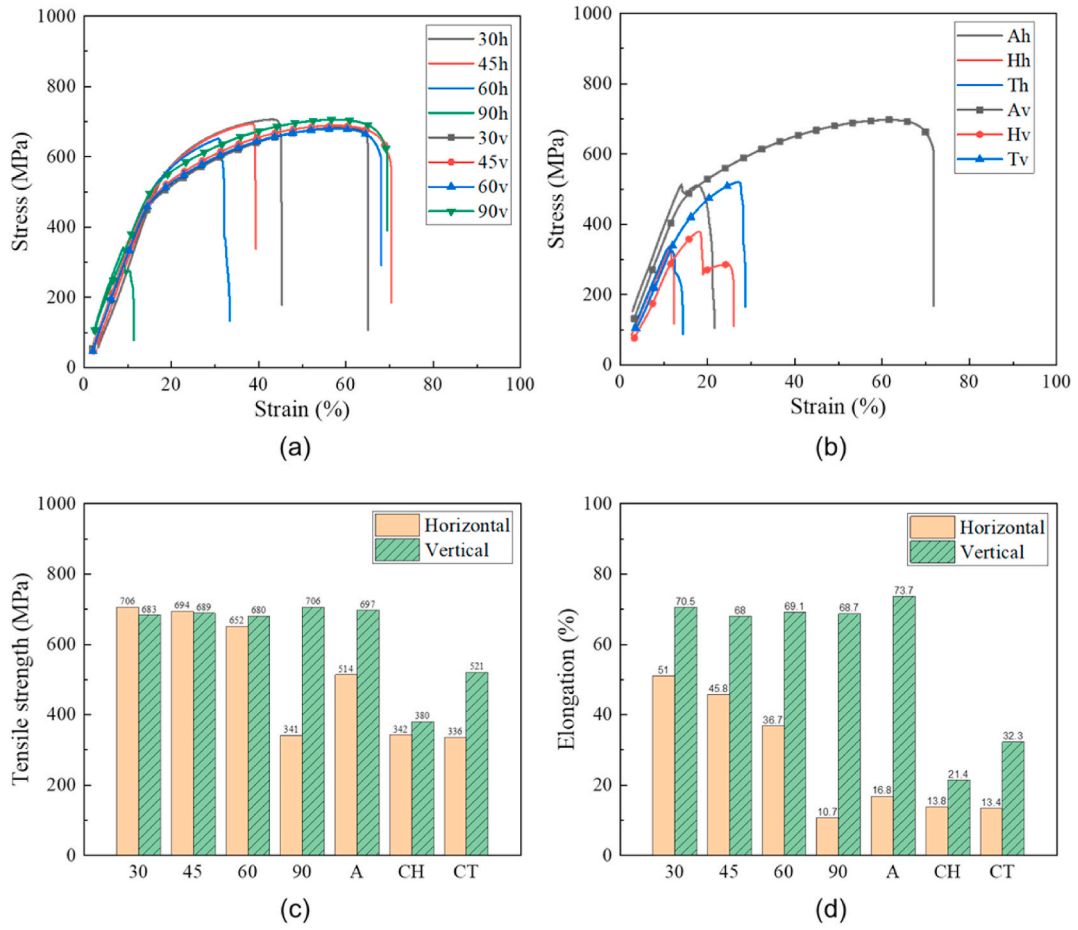

Fig. 9. Tensile test results: (a) stress–stain curve of V-type specimens; (b) stress–stain curve of anchor, T, and hammer specimens; (c) tensile strength; and (d) elongation.

magnification views in Figs. 10 d-1, e−1 and f-1. However, the horizontally laminated specimens exhibit unique fracture surface characteristics. In Fig. 10 (a), Chevron patterns are observed at the tip of the V, as shown in a-1, and the same ductile fracture surface is observed in a-2. The large-scale fracture surfaces observed in Fig. 10 a-1 are typically observed in b-1. Complex fracture patterns, including dimple and Chevron patterns, are observed. However, a limited number of dimples are observed; therefore, it is reasonable to assume that this surface is a brittle fracture-dominant surface. Conversely, a typical ductile fracture surface is observed in Figs. 10 b-2. Fig. 10 (c) shows a fracture surface similar to that shown in Fig. 10 (b), which cannot be distinguished without the angle of the brittle fracture-dominant surface by the fractographies shown in Fig. 10 c-1 and c-2. When $\theta_V = 90\ ^\circ$, the worst situation occurs, as shown in Fig. 10 (g). It is clear that the giant crack resembles a cliff, as shown in Fig. 10 (g) g-1. The "cliff" is a critical obstruction, such that even traces of the conjunction are difficult to detect from the fracture surface.

Among the horizontal V-type specimens, the fracture surfaces have quite clear distinctions between specific θ_Vs. When $\theta_V < \frac{\pi-\theta_P}{2}$, the most critical point is the tip of the V because this point fractures at the beginning, as shown in Fig. 8 (a), and deformed and undeformed pores are observed in Fig. 10(a) a-1. This indicates that relatively minor defects are concentrated at this point. When $\theta_V \approx \frac{\pi-\theta_P}{2}$ or $\theta_V > \frac{\pi-\theta_P}{2}$, the most critical point moves to the interface between the two materials. It fractures at the beginning of its course, in Fig. 8 (a) and (b), and numerous pores and cracks are observed in Fig. 10 b-1 and c-1. The critical interfaces exhibit some similarities, wherein they are always generated when 316L is laminated on In625, and they are always located over the other interface during AM. This implies that there are several reasons as to why they have become critical.

First, defects are generated because of the obstacle effect when $\theta_V \geq \frac{\pi-\theta_P}{2}$, as schematically shown in Fig. 1. This is discussed in **Section 2**. Second, less mass is laminated. During AM, the previously laminated material flattens because of the heat input and the increase in mass due to the laminated metal. This aids the material conjunction because heat energy decreases its strain energy, and gravity provides potential energy. The critical surfaces lack energy for conjunction when compared to the other surfaces. Therefore, the vertically laminated specimens have no fracture surfaces along the interface.

Similarly, this explains why the tip of the V is a critical point when $\theta_V = 30\ ^\circ$. When $\theta_V < \frac{\pi-\theta_P}{2}$, the interface is no longer critical because the previously laminated slope is no longer an obstacle. Additionally, the upper directional lamination is dominant in aiding

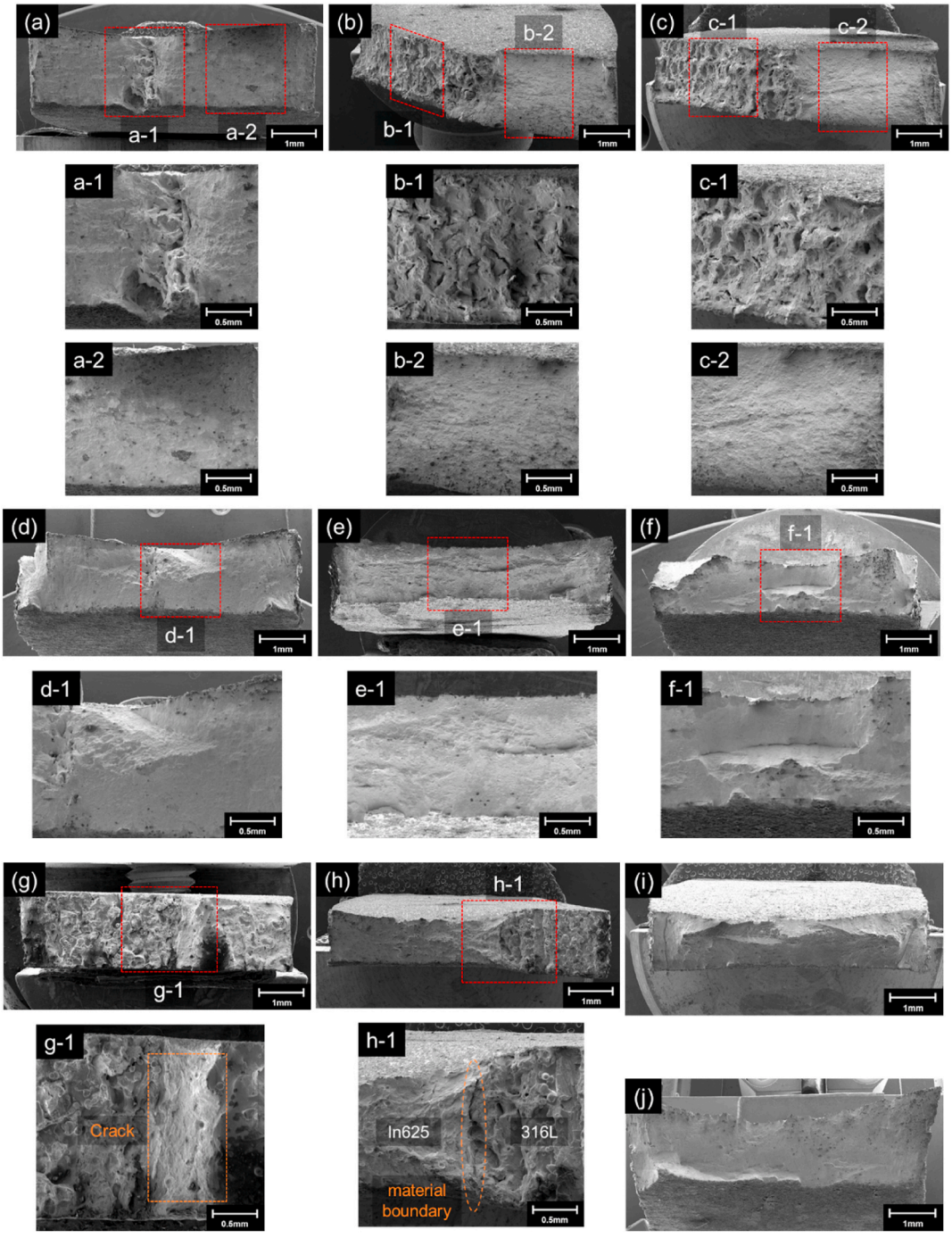

Fig. 10. Fracture surface observed by SEM: (a) horizontal V-type specimens at 30°, (b) 45°, (c) 60° and (d) vertical V-type specimens at 30°, (e) 45°, (f) 60°; (g) horizontal simple bonding specimen; (h) anchor specimen; (i) vertical simple bonding specimen; and (j) vertical anchor specimen.

the interface in achieving good quality when θ_V is small. This is because it provides a greater portion of gravity and heat. Therefore, the conjunction quality of $\theta_V = 30\ ^\circ$ is better than that of others. Finally, the tip of the V is the weakest point due to the shrinkage by solidification. Following the sequence introduced in Fig. 2, the layer where the tip is located is completely laminated after fabricating all the In625 parts. During the lamination of the In625 part, the layer corresponding to the tip shrinks because of its solidification residual stress and that of the laminated layers above it [36]. Therefore, there is a gap between the two materials in this layer.

In the case of the anchor, as shown in Fig. 10 (h), a novel point can be observed: the fracture surface of the In625. A material interface is observed, as shown in Fig. 10 (h) h-1. It can be inferred that the In625 site is located on the left side of the boundary.

However, it is difficult to distinguish these two materials using SEM images without an interface. With the exception of the fractured surface of the interface, the remaining surfaces are ductile fracture surfaces. Plastic deformation is accompanied by mass and long-range material transfer until ductile fracture occurs. Therefore, it is possible to fill the material boundaries during plastic deformation.

The reasons for the occurrence of In625 fractures are as follows: when the angle of V on the edge is 60°, interfacial fracture occurs first, as shown in Fig. 8 (h), which is the principle observed in all V specimens whose $\theta_V > \frac{\pi-\theta_P}{2}$. Then, the remaining area of the fractured section decreases to 2/3, and theoretically, the geometric axis moves to the side. Here, the section challenges both the increased stress and bending moment generated by the mismatch of the geometric axes. The bending moment can be calculated as the increase in stress on the In625 side and the decrease in the stress on the other side. Therefore, the fracture of In625 is bound to occur according to the Euler–Bernoulli beam theory. Up to this point, the discussion has primarily focused on the experimental results. Hence, the validation section is presented next.

The interface is critical in specific specimens because of defects that occur during lamination. As an intuitive method, the OM is used to validate the results, as shown in Fig. 11. The size and number of defects are critical characteristics that determine the conjunction quality. Given that the number of defects cannot be determined accurately by counting the number of defects in the figure, it is reasonable to focus on the size of the defects. A comparison of the sizes of defects on the critical interface (upper interface), according to θ_V, is presented in Fig. 11 (a), (b), and (c); the biggest one is observed at 60°. Additionally, a crack is detected at the interface, which causes an interfacial fracture at 45°. Critical defects are detected in both materials, as shown in Fig. 11 (d). In the case of the anchor, critical defects, including cracks and pores, are detected at the horizontal interface, as shown in Fig. 11 e−1 and e−2.

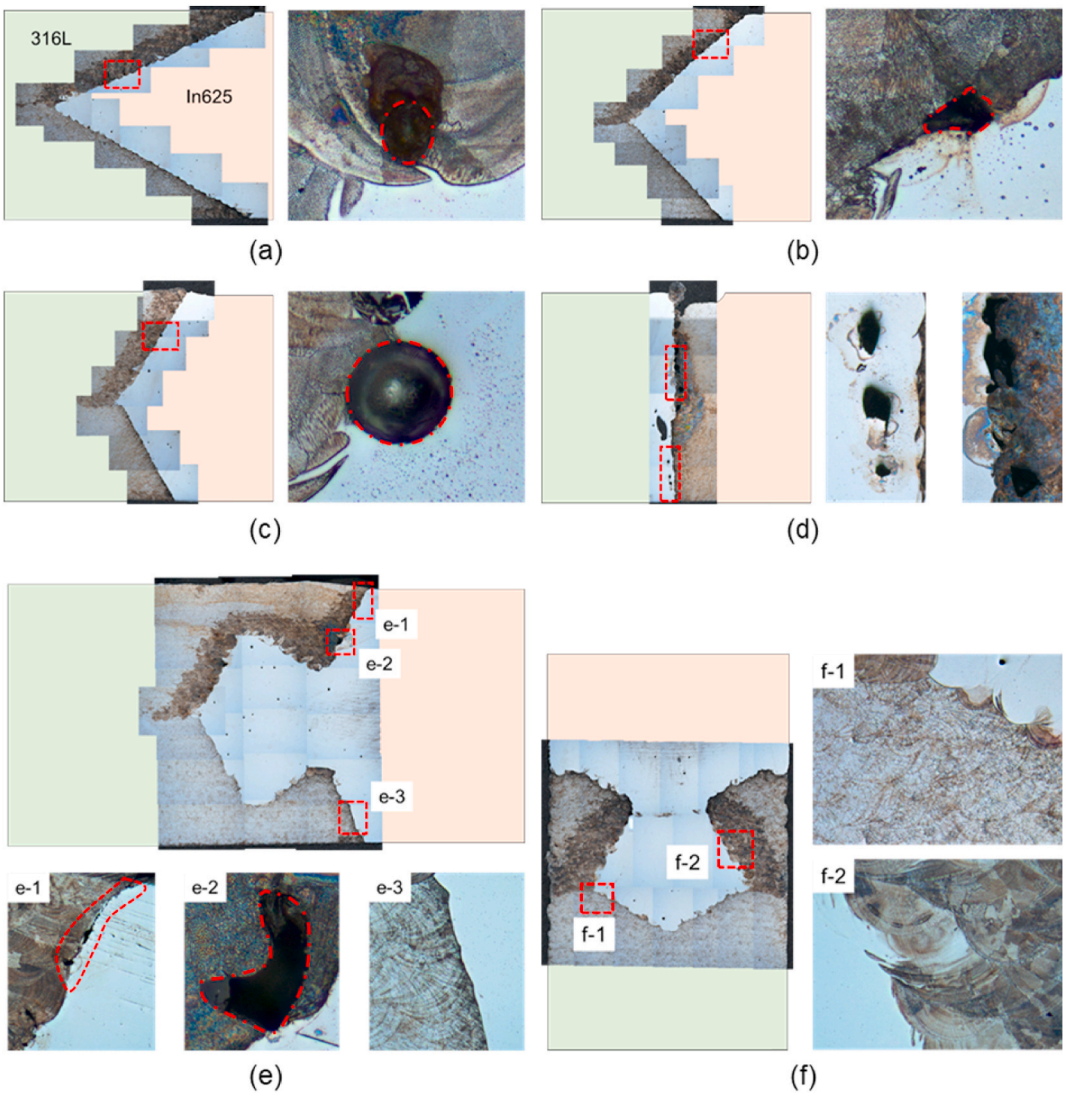

Fig. 11. OM images of MMAM specimens: (a) V-types with $\theta_V = 30°$, (b) 45°, and (c) 60°; (d) horizontal simple bonding specimens; (e) anchors; and (f) vertical anchor.

However, interfaces without defects are observed on the other side of the interface and vertical anchor, as shown in Fig. 11 e−3 and (f), respectively.

This indicates that an ideal anchor that can connect mechanically, even though the materials are entirely different, can be fabricated by changing the design. The most commonly used metal materials are alloys, and different compositions exhibit different characteristics. The demand for advanced materials with various characteristics increases as technology advances. However, different materials, such as aluminum and steel, have different characteristics. Therefore, an anchor that can solve this problem exhibits excellent potential for application in many areas, such as aerospace, automobiles, and defense.

To validate the tensile test results, the displacement of the sample is analyzed using DIC, as shown in Fig. 12. The DIC figures show the strains when the specimens reach the maximum load, as shown in tensile curves presented in Fig. 9 (a) and (b). In the case of V-type specimens, except for horizontal simple bonding ($\theta_V = 90°$), the maximum load points are located on the curves of plastic deformation followed by elastic deformations. In the case of complex interface geometries of anchor, only the vertical anchor was fractured after pronounced plastic deformation whereas the fractures occurred in sudden drops after relatively small deformation in all the other cases. In the case of horizontal V-type specimens, the strain is detected with clear increments as θ_V decreases, as shown in Fig. 12 (a). This figure shows the strain fields measured from the horizontal V-type specimens when they reach the maximum load. The normal strain components in two different directions, parallel and perpendicular to the tensile direction (ε_{xx} and ε_{yy}), indicate that severely localized deformation occurs in the 316L part, regardless of θ_V. These local deformations generate a concentrated shear stress region near the two edges of the interfaces, as shown by ε_{xy} in the figure. The region where localized shear strain occurs becomes narrower upon increasing θ_V, indicating the stress concentration. This behavior is probably due to the poorer interface connection between the two materials at high θ_V. However, the mechanism used for the horizontal specimens is no longer applicable to the vertical specimens, as shown in Fig. 12 (b). This figure shows the strain fields measured from the vertical specimens when they reach their maximum loads. This appears to be a conventional single-material tensile test result. The shear stress is no longer concentrated near the interface but in the 316L part. There is no relationship between stress concentration and θ_V. These phenomena validate the difference in tensile strength and elongation shown in Fig. 9. The tensile strength and elongation of V-type specimens are shown to be much higher than those of horizontal simple bonding, T-type and hammer type specimens. Because they are considered to have no critical defects generated by the obstacle effect. These results are considered to be purely by the designs and lamination strategies, having no relationship with interactions between the materials such as 316L and In625 which were used in this study. Therefore, the same effect is expected when the developed strategy is applied to other alloys combinations.

Notably, the asymmetrical strain detected in Fig. 12 (a) is horizontal because the asymmetry is located at the interface. Here, the incomplete ductile fracture, which is observed in Fig. 10 (b) and (c), is validated because the asymmetrical strains are clearer at 45° and 60° than at 30° and the verticals. A much more contrasting result is shown in the simple horizontal bonding ($\theta_V = 90°$) in Fig. 12 (c), which shows a complete brittle deformation. The deformations are too small to distinguish their normal direction, and only the rotation is sufficiently clear to specify its stress concentration point and fracture starting point. However, the vertical simple bonding specimen shows a typical deformation distribution of a well-welded heterogeneous material with different mechanical performances.

In the case of the anchor, unique strain deposition is detected, as shown in Fig. 12 (d). The figure shows the strain fields of the anchor when it reaches the maximum load. However, no detectable cracks are observed. When the anchor works well (vertical), most of the strain occurs in the 316L part, which indicates that it is the weakest section in the entire specimen. However, if it is not (in the case of horizontal), it is only applicable up to a certain point. The normal strain along the x-axis exhibits a clearly unusual behavior and is concentrated at the critical interface. However, a normal strain along the y-axis occurs in the 316L part, which is slightly below the conjunction in the specimen. This validates the performance of the anchor and the occurrence of fractures. Finally, the strain of rotation confirms that the interface is ready and set to fracture. The strain occurs because the direction of the interfacial fracture is normal to that of the interface. This validates that a bending moment exists before the interfacial fracture and that it causes critical damage to the anchor.

6. Conclusions

In this study, a V-shaped design developed for dense multi-material AM was manufactured at angles below, near, and above the obstruction angle. The performance varied according to the building direction and angle θ_V. The performance of the V-type conjunction initially varied according to the building direction. The vertical V-type appeared to have no direct relation with θ_V, and the V-type specimen performed similarly in both strength and elongation if it exceeded or failed to meet the limit. Conversely, for horizontal lamination, a limit for θ_V exists, which influences the performance and conjunction quality of the V-type structure. When it did not exceed the limit, the V-type structure exhibited better performance in terms of both strength and elongation, with a decrease in θ_V. When θ_V exceeded the limit, defects, including pores and cracks, occurred at the interface of the two materials, which dominantly decided the quality of the V-type. The defects increased and became more critical when θ_V increased. This was prominent in the case of simple-type specimens, including horizontal simple bonding, T, and hammer specimens. It was estimated to be a clear manufacturing failure if the measured maximum strength was less than half the performance of LDED-processed 316L and the maximum elongation was one-fourth that of LDED-processed 316L. This was obtained via the tensile test with DIC and fracture surface analysis via SEM and OM on the surface of the untested specimens.

The V-type characteristics are still available for anchor which is developed using a combination of three V-type joints for mechanically interlocking dissimilar materials. Consequently, the vertical anchor joint performed perfectly as anticipated, with its performance matching that of other vertical specimens that also exhibited flawless execution. However, the horizontal anchor failed to

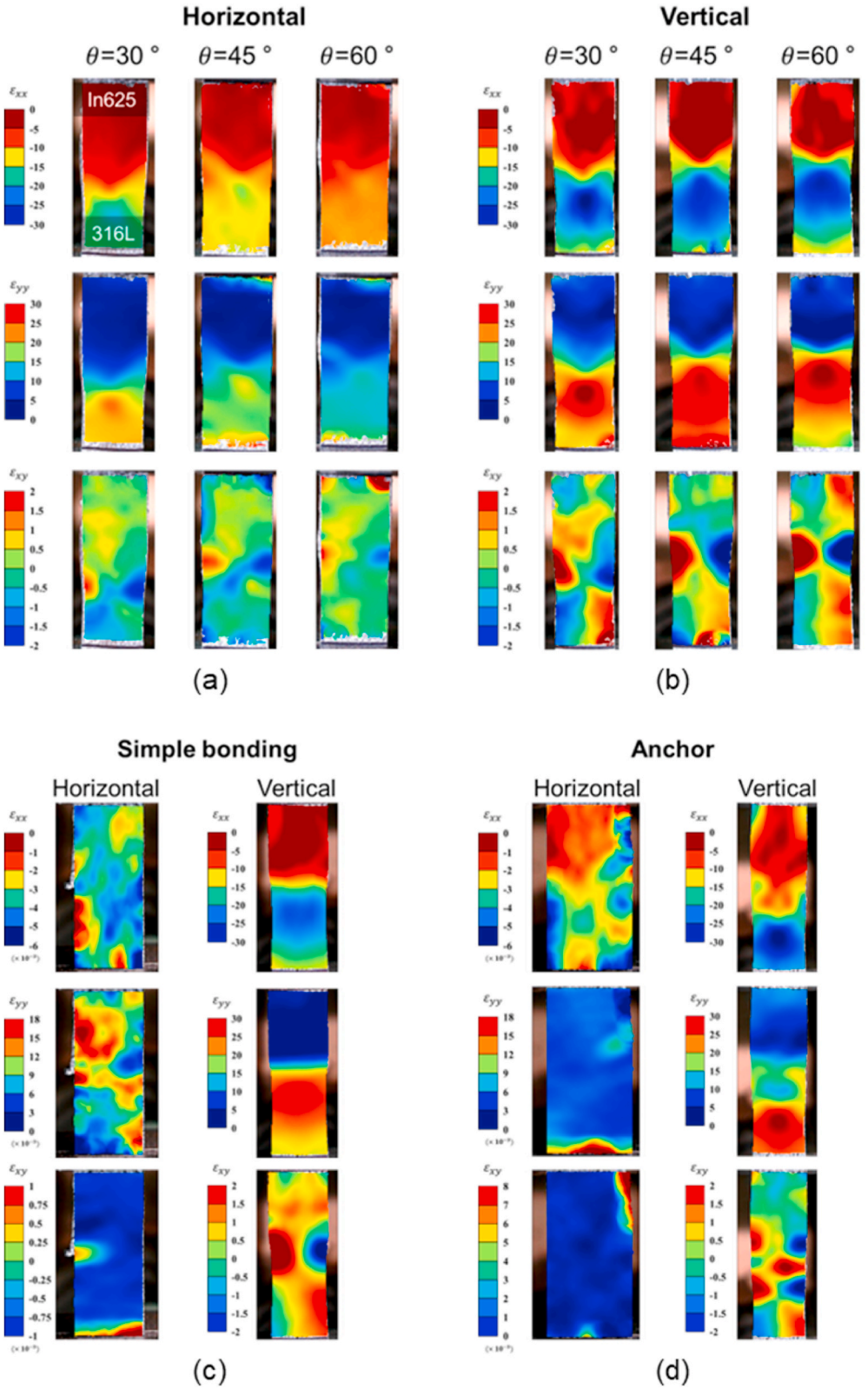

Fig. 12. DIC results showing strain fields in the X, Y, and XY directions when they are at the maximum load on (a) V-type horizontal specimens, (b) vertical specimens, (c) horizontal and vertical simple bonding specimens, and (d) anchor specimens.

maintain its functionality during the tensile test. In the case of T-type and hammer type specimens whose interface geometries are T shaped and hammer shaped, no matter their building direction, the performances are far fall behind than the anchor. The result is reasonable since their designs of interface geometry avoid obstacle effect, which generate many critical defects.

In the case of horizontal anchor, since the design of interface geometry seems to have slopes which can avoid obstacle effect, however a small defect existed in the interface where the lamination of last layers ended. Following the same principles, the defect was generated because the angle exceeds the permissible limit. This interface is the primary cause of its unsatisfactory performance. In contrast, the vertical anchor shows satisfactory results, demonstrating strength and elongation similar to that of LDED-processed 316L, suggesting that the anchor's performance can be enhanced via design optimization. Since this improved performance is purely because of the design and lamination strategy, it is expected that the same improvement can be obtained when the developed strategy is applied on other joints which connect other alloys combinations. Future research on anchors for MMAM will focus on several key areas: adjusting the problematic angle, developing features more efficiently, and implementing continuous anchor connections for large-scale applications.

Funding

This work was supported by the National Research Foundation of Korea under grant number 2022R1A2C1012478, and was co-supported by the Advanced Technology Center Development Program (Grant No. 20008753) funded by the Ministry of Trade, Industry & Energy (MOTIE, Korea), which are gratefully acknowledged.

Data availability statement

The data that support the findings of this study are available from the corresponding authors, upon reasonable request.

CRediT authorship contribution statement

Qing-Ye Jin: Writing – original draft, Investigation, Formal analysis. **Hyunji Nam:** Methodology, Investigation. **Haeju Jo:** Methodology, Investigation. **Jiyoung Park:** Methodology, Investigation. **Ho Ju Kang:** Validation, Resources. **Dong Joo Kim:** Project administration. **Wookjin Lee:** Writing – review & editing, Conceptualization.

Declaration of competing interest

The authors declare that they have no known competing financial interests or personal relationships that could have appeared to influence the work reported in this paper.

References

[1] D. Rosen, S. Kim, Design and manufacturing implications of additive manufacturing, J. Mater. Eng. Perform. 30 (2021) 6426–6438, https://doi.org/10.1007/s11665-021-06030-6.
[2] Y. Han, W.F. Lu, A novel design method for nonuniform lattice structures based on topology optimization, J. Mech. Des. Trans. ASME. 140 (2018) 1–10, https://doi.org/10.1115/1.4040546.
[3] A.O. Aremu, J.P.J. Brennan-Craddock, A. Panesar, I.A. Ashcroft, R.J.M. Hague, R.D. Wildman, C. Tuck, A voxel-based method of constructing and skinning conformal and functionally graded lattice structures suitable for additive manufacturing, Addit. Manuf. 13 (2017) 1–13, https://doi.org/10.1016/j.addma.2016.10.006.
[4] C. Liu, Z. Du, W. Zhang, Y. Zhu, X. Guo, Additive manufacturing-oriented design of graded lattice structures through explicit topology optimization, J. Appl. Mech. Trans. ASME. 84 (2017) 1–12, https://doi.org/10.1115/1.4036941.
[5] C. Yan, L. Hao, A. Hussein, P. Young, D. Raymont, Advanced lightweight 316L stainless steel cellular lattice structures fabricated via selective laser melting, Mater. Des. 55 (2014) 533–541, https://doi.org/10.1016/j.matdes.2013.10.027.
[6] R. Kosturek, M. Wachowski, L. Śnieżek, M. Gloc, The influence of the post-weld heat treatment on the microstructure of inconel 625/carbon steel bimetal joint obtained by explosive welding, Metals 9 (2) (2019) 246, https://doi.org/10.3390/met9020246.
[7] Y. Li, P. Podaný, M. Koukolíková, J. Džugan, T. Krajňák, J. Veselý, S. Raghavan, Effect of heat treatment on creep deformation and fracture properties for a coarse-grained inconel 718 manufactured by directed energy deposition, Materials 16 (2023), https://doi.org/10.3390/ma16041377.
[8] M. Yu, A. Feng, L. Yang, M.E. Thomas, Microstructure and corrosion behaviour of 316 L-IN625 functionally graded materials via laser metal deposition, Corrosion Sci. 193 (2021) 109876, https://doi.org/10.1016/j.corsci.2021.109876.
[9] N. Alloy, Z. Tian, C. Zhang, D. Wang, W. Liu, X. Fang, A review on laser powder bed fusion of inconel 625, Appl. Sci. 10 (1) (2020) 81, https://doi.org/10.3390/app10010081.
[10] F. Zafar, O. Emadinia, M. Vieira, A. Reis, A Review on Direct Laser Deposition of Inconel 625 and Inconel 625-Based Composites—Challenges and Prospects, Metals 13 (4) (2023) 787, https://doi.org/10.3390/met13040787.
[11] M. Karmuhilan, S. Kumanan, A review on additive manufacturing processes of inconel 625, J. Mater. Eng. Perform. 31 (2022) 2583–2592, https://doi.org/10.1007/s11665-021-06427-3.
[12] V.B. Vukkum, R.K. Gupta, Review on corrosion performance of laser powder-bed fusion printed 316L stainless steel: effect of processing parameters, manufacturing defects, post-processing, feedstock, and microstructure, Mater. Des. 221 (2022) 110874, https://doi.org/10.1016/j.matdes.2022.110874.
[13] M.J.K. Lodhi, K.M. Deen, M.C. Greenlee-Wacker, W. Haider, Additively manufactured 316L stainless steel with improved corrosion resistance and biological response for biomedical applications, Addit. Manuf. 27 (2019) 8–19, https://doi.org/10.1016/j.addma.2019.02.005.
[14] A. Saboori, A. Aversa, G. Marchese, S. Biamino, M. Lombardi, P. Fino, Microstructure and mechanical properties of AISI 316L produced by directed energy deposition-based additive manufacturing: a review, Appl. Sci. 10 (2020), https://doi.org/10.3390/app10093310.
[15] S. Hasanov, S. Alkunte, M. Rajeshirke, A. Gupta, O. Huseynov, I. Fidan, F. Alifui-Segbaya, A. Rennie, Review on additive manufacturing of multi-material parts: progress and challenges, J. Manuf. Mater. Process. 6 (2022), https://doi.org/10.3390/jmmp6010004.

[16] T.A. Rodrigues, F.W. Cipriano Farias, K. Zhang, A. Shamsolhodaei, J. Shen, N. Zhou, N. Schell, J. Capek, E. Polatidis, T.G. Santos, J.P. Oliveira, Wire and arc additive manufacturing of 316L stainless steel/Inconel 625 functionally graded material: Development and characterization, J. Mater. Res. Technol. 21 (2022) 237–251, https://doi.org/10.1016/j.jmrt.2022.08.169.
[17] A. Nazir, O. Gokcekaya, K. Md Masum Billah, O. Ertugrul, J. Jiang, J. Sun, S. Hussain, Multi-material additive manufacturing: a systematic review of design, properties, applications, challenges, and 3D printing of materials and cellular metamaterials, Mater. Des. 226 (2023) 111661, https://doi.org/10.1016/j.matdes.2023.111661.
[18] B. Heer, A. Bandyopadhyay, Compositionally graded magnetic-nonmagnetic bimetallic structure using laser engineered net shaping, Mater. Lett. 216 (2018) 16–19, https://doi.org/10.1016/j.matlet.2017.12.129.
[19] N.E. Putra, M.J. Mirzaali, I. Apachitei, J. Zhou, A.A. Zadpoor, Multi-material additive manufacturing technologies for Ti-, Mg-, and Fe-based biomaterials for bone substitution, Acta Biomater. 109 (2020) 1–20, https://doi.org/10.1016/j.actbio.2020.03.037.
[20] M.J. Sagong, E.S. Kim, J.M. Park, G.M. Karthik, B.J. Lee, J.W. Cho, C.S. Lee, T. Nakano, H.S. Kim, Interface characteristics and mechanical behavior of additively manufactured multi-material of stainless steel and Inconel, Mater. Sci. Eng. 847 (2022) 143318, https://doi.org/10.1016/j.msea.2022.143318.
[21] D. Melzer, J. Džugan, M. Koukolíková, S. Rzepa, J. Vavřík, Structural integrity and mechanical properties of the functionally graded material based on 316L/IN718 processed by DED technology, Mater. Sci. Eng. 811 (2021), https://doi.org/10.1016/j.msea.2021.141038.
[22] X. Zhang, Y. Chen, F. Liou, Fabrication of SS316L-IN625 functionally graded materials by powder-fed directed energy deposition, Sci. Technol. Weld. Join. 24 (2019) 504–516, https://doi.org/10.1080/13621718.2019.1589086.
[23] Y. Li, T. Krajňák, P. Podaný, J. Veselý, J. Džugan, Thermal stability of dislocation structure and its effect on creep property in austenitic 316L stainless steel manufactured by directed energy deposition, Mater. Sci. Eng. 873 (2023), https://doi.org/10.1016/j.msea.2023.144981.
[24] D. Melzer, J. Gil, S. Rzepa, R. Amaral, P. Podaný, J. Džugan, A. Reis, Ambient and high temperature tensile behaviour of DLD-manufactured inconel 625/42C steel joint, Mater. Sci. Eng. 885 (2023), https://doi.org/10.1016/j.msea.2023.145603.
[25] D. Melzer, M. Koukolíková, S. Rzepa, Y. Li, J. Džugan, M. Brázda, Influence of interface orientation and surface quality on structural and mechanical properties of SS316L/IN718 block produced using directed energy deposition, Surface. Interfac. 41 (2023), https://doi.org/10.1016/j.surfin.2023.103139.
[26] M. Arza-García, C. Núñez-Temes, J.A. Lorenzana, J. Ortiz-Sanz, A. Castro, M. Portela-Barral, M. Gil-Docampo, G. Bastos, Evaluation of a low-cost approach to 2-D digital image correlation vs. a commercial stereo-DIC system in Brazilian testing of soil specimens, Arch. Civ. Mech. Eng. 22 (2022) 1–13, https://doi.org/10.1007/s43452-021-00325-0.
[27] E. Azinpour, R. Darabi, J. Cesar de Sa, A. Santos, J. Hodek, J. Dzugan, Fracture analysis in directed energy deposition (DED) manufactured 316L stainless steel using a phase-field approach, Finite Elem, Anal. Des. 177 (2020) 103417, https://doi.org/10.1016/j.finel.2020.103417.
[28] A. Li, X. Liu, X. Wan, Y. Yang, Thermal behaviors and fluid flow controlling the geometry of 7075 aluminum alloy single tracks during liquid metal flow rapid cooling additive manufacturing, Int. Commun. Heat Mass Transf. 116 (2020) 104664, https://doi.org/10.1016/j.icheatmasstransfer.2020.104664.
[29] Z. Gan, G. Yu, X. He, S. Li, Surface-active element transport and its effect on liquid metal flow in laser-assisted additive manufacturing, Int. Commun. Heat Mass Transf. 86 (2017) 206–214, https://doi.org/10.1016/j.icheatmasstransfer.2017.06.007.
[30] Y. Zhou, W. Qu, F. Zhou, X. Li, L. Song, Q. Zhu, Thermo-fluid flow behavior of the IN718 molten pool in the laser directed energy deposition process under magnetic field, Rapid Prototyp. J. 29 (2023) 460–473, https://doi.org/10.1108/RPJ-05-2022-0143.
[31] Z. Li, G. Yu, X. He, S. Li, Z. Shu, Surface tension-driven flow and its correlation with mass transfer during L-DED of Co-based powders, Metals 12 (2022), https://doi.org/10.3390/met12050842.
[32] H. Nam, Q. Jin, J. Park, W. Lee, Effect of process parameter and scanning strategy on the microstructure and mechanical properties of inconel 625 superalloy manufactured by laser direct energy deposition, Korean J. Met. Mater. 61 (2023) 772–784, https://doi.org/10.3365/KJMM.2023.61.10.772.
[33] J. Park, H. Nam, Q. Jin, W. Lee, Effects of process parameters on the dimensions and mechanical properties of L-DED AISI 316L stainless steel, Korean J. Met. Mater. 61 (2023) 760–771, https://doi.org/10.3365/KJMM.2023.61.10.760.
[34] P. Cheng, M.A. Sutton, H.W. Schreier, S.R. McNeill, Full-field speckle pattern image correlation with B-Spline deformation function, Exp. Mech. 42 (2002) 344–352, https://doi.org/10.1007/bf02410992.
[35] H.A. Bruck, S.R. McNeill, M.A. Sutton, W.H. Peters, Digital image correlation using Newton-Raphson method of partial differential correction, Exp. Mech. 29 (1989) 261–267, https://doi.org/10.1007/BF02321405.
[36] Q.Y. Jin, D. Kang, K. Ha, J.H. Yu, W. Lee, Simulation of annealing process on AISI 316 L stainless steel fabricated via laser powder bed fusion using finite element method with creep, Addit. Manuf. 60 (2022) 103255, https://doi.org/10.1016/j.addma.2022.103255.